ADVANCED MATERIALS
www.advmat.de

Self-Manipulating Sodium Ion Gradient-Based Endogenic Electrical Stimulation Dressing for Wound Repair

Ruizeng Luo, Yijie Fan, Yilin Qi, Yuan Bai, Meng Xiao, Yujia Lv, Jinrui Liang, Mingcheng Tang, Jiaping Zhang, Zhou Li,* and Dan Luo**

Endogenous electric field (EF) originating from differences in ionic gradients plays a decisive role in the wound healing process. Based on this understanding, a self-manipulating sodium ion gradient-based endogenic electrical stimulation dressing (smig-EESD) is developed to achieve passive, non-invasive, endogenic electrical stimulation of wounds, which avoids the side effects of electrode occupancy, electrochemical reactions, and thermal effects present in traditional exogenous electrical stimulation. smig-EESD reduced the potential at the center of the wound by specifically absorbing Na+ in the exudate, ultimately strengthening the wound endogenous EF. Importantly, smig-EESD converted the active transport dependent on Na^+/K^+-ATPase into passive diffusion by adsorbing extracellular matrix Na+, and the saved ATP consumption promoted tissue repair process. smig-EESD regulated innate and adaptive immune responses by upregulating the secretion of multiple cytokines, thereby suppressing injury-associated inflammatory responses and reducing scar formation. smig-EESD reveals an endogenic electrical stimulation strategy that is independent of electrodes and circuits, and provides new insights into the future development of electronic medicine.

1. Introduction

As the first barrier of the human body, the skin can protect the internal tissues from external physical, chemical or biological factors. However, the skin is extremely vulnerable, and chronic wounds and large open wounds have become a serious global public health problem that affects millions of people every year.[1] Any damage to the skin should be repaired quickly and efficiently. Generally, the skin wound healing process is promoted by multiple factors, such as injury stimulation, induction of biochemical factors,[2] inflammatory response,[3] and wound endogenous electric field (EF).[4] Among them, wound endogenous EF is an extremely important and indispensable factor in wound healing. Since wound endogenous EF can promote the proliferation of epithelial cells and induce their migration from the wound edge to the defective tissue, the attenuation of endogenous EF will prolong the wound healing time and hinder the re-epithelialization of the skin.[5]

Wound endogenous EF is generated by the short circuit of the normal epidermal transepithelial potential (TEP) caused by trauma, and its essence is derived from the gradient distribution of ions.[5a] The formation of TEP is closely related to the asymmetric distribution of ion channels in epidermal cells, that is, Na^+ channels (inward flow) and Cl^- channels (outward flow) are located at the apical plasma membrane, and K^+ channels (outward flow) are located at the basal plasma membrane together with Na^+/K^+-ATPase (outward flow of Na^+ and inward flow of K^+).[6] In normal epidermal tissue, the tight junction between the epidermal cells prevents the flow of ions in the intercellular space, which leads to the accumulation of Cl^- at the apical plasma membrane of the epidermal

R. Luo, Y. Fan, Y. Qi, Y. Bai, M. Xiao, Y. Lv, Z. Li, D. Luo
Beijing Institute of Nanoenergy and Nanosystems
Chinese Academy of Sciences
Beijing 101400, China
E-mail: zli@binn.cas.cn; luodan@binn.cas.cn

R. Luo, Z. Li
Beijing Tsinghua Changgung Hospital
School of Clinical Medicine
School of Biomedical Engineering
Tsinghua Medicine
Tsinghua University
Beijing 100084, China

The ORCID identification number(s) for the author(s) of this article can be found under https://doi.org/10.1002/adma.202419149

DOI: 10.1002/adma.202419149

R. Luo, M. Tang, J. Zhang, Z. Li
Department of Plastic Surgery
State Key Laboratory of Trauma
Burns and Combined Injury
Southwest Hospital
Third Military Medical University (Army Medical University)
Chongqing 400038, China
E-mail: japzhang@aliyun.com

R. Luo, Y. Fan, Y. Qi, M. Xiao, Z. Li
School of Nanoscience and Engineering
University of Chinese Academy of Sciences
Beijing 100049, China

Y. Bai, Z. Li
Center on Nanoenergy Research
School of Physical Science & Technology
Guangxi University
Nanning 530004, China

cells and the accumulation of Na^+ at the basal plasma membrane, thereby forming a electric potential difference from the basal side to the apical side of the epithelial tissue (TEP).[7] Once the intact epithelial tissue is destroyed, the tight junctions are interrupted, creating a short circuit at the wound site. The high concentration of Na^+ accumulated at the basal side of the surrounding normal epithelium is discharged to the wound site to form a potential difference caused by the cation concentration gradient; while Cl^- flows into the basal side of the epithelial tissue through the low-resistance wound site to neutralize the Na^+ at the wound center, further enhancing the potential difference, and ultimately generating an endogenous electric field from the wound edge (anode) to the wound center (cathode).[6]

Exogenous electrical stimulation devices have been proven to simulate or enhance the wound endogenous EF by outputting voltage (or current), thereby promoting wound healing.[8] However, exogenous electrical stimulation devices cannot be separated from the integration of power supply and electrodes. Although the electrical stimulation therapy devices have been miniaturized and integrated, the additional power supply not only increases the processing cost of the device,[9] but also the risk of leakage of harmful components in energy storage modules such as batteries; and the electrodes will produce a space-occupying effect and induce inflammatory response, hindering wound healing. In addition, the current generated by electronic devices are usually transmitted in the form of electrons. When the electronic current acts on the skin wound, it needs to be converted into endogenous ionic current, accompanied by electrochemical reactions and thermal effects,[10] thereby causing secondary damage to the skin tissue. This dilemma emphasizes the importance of developing innovative bioelectric stimulation technologies that are independent of power supplies and electrodes and can self-manipulate endogenous cation gradients.

Previous studies have confirmed that the ions in wound exudate are mainly Na^+ and Cl^-, which are the same types of ions that maintain TEP and endogenous EF.[11] It can be inferred that the regulation of endogenous EF can be achieved by manipulating the ions of exudate: by specifically adsorbing Na^+ to expand the cation gradient from the wound periphery to the center, while physically isolating the adsorption of anions to enrich them in the wound center; it is expected to form a more negative potential in the wound center, thereby strengthening the wound's ionic current and forming a stronger endogenous EF. Inspired by this, we have developed a self-manipulating sodium ion gradient-based endogenic electrical stimulation dressing (smig-EESD) to address the growing clinical demand for the treatment of large or chronic full-layer skin wounds (**Figure 1**). The selective ion manipulation capability of smig-EESD originates from its core component, hard carbon (HC) formed by high-temperature pyrolysis of ginkgo leaves.[12] As a biocompatible Na^+ storage material, HC selectively adsorbs or embeds hydrated Na^+ ions based on the mechanism of "adsorption, filling, and intercalation", using defects on its surface and edges, interstices between graphite layers, and micropores formed between randomly oriented graphite; while potassium ions (K^+) and chloride ions (Cl^-) cannot be adsorbed or bound by HC due to size mismatch.[13] smig-EESD could absorb Na^+ in wound exudate and create a more negative potential in the wound center; as evidenced by wound potential measurements, smig-EESD significantly enhanced endogenous EF of wounds. Animal experiments showed that endogenic electrical stimulation produced by smig-EESD shortened the entire wound repair process, and promoted wound healing. Notably, smig-EESD also intervened in the ATP-mediated ion transport process: the adsorption of smig-EESD reduced the content of Na^+ in the extracellular matrix, so the process of epithelial cells transporting Na^+ from the cell to the extracellular space was transformed from active transport against the concentration gradient to passive diffusion along the concentration gradient, thereby reducing the energy consumption of the Na^+/K^+-ATPase. The saved ATP consumption faciliated promoting cell proliferation and migration during tissue repair. In summary, smig-EESD enhanced endogenous EF of the wound by regulating ionic gradient in a passive and noninvasive manner, which perfectly accelerated almost all necessary stages of wound repair and has a broad clinical prospect.

2. Results and Discussion

2.1. Materials, Structure and Performance Characteristics of the smig-EESD

smig-EESD was composed of polyurethane (PU) and HC: polyurethane is waterproof and prevents the invasion of microorganisms, providing a moist wound healing environment; HC can manipulate the sodium ion gradient, thereby enhancing endogenous EF. HC was fabricated by annealing ginkgo biloba leaves at high temperatures in a nitrogen atmosphere. HC prepared at temperatures above 800 °C is considered to have sodium storage capacity.[12] In order to obtain the HC with the strongest sodium storage capacity, we tried to synthesize HC at different pyrolysis temperatures (900, 1100, and 1300 °C), and characterized its nanostructure and crystallinity by high-resolution transmission electron microscopy (HRTEM), X-ray diffraction (XRD), and Raman spectroscopy (**Figure 2a–d**). HRTEM images showed that with the increase of pyrolysis temperature, the microcrystalline structure of carbon gradually changed from a highly disordered phase to a graphite-like phase (Figure S1, Supporting Information). When the pyrolysis temperature raised to 1100 °C, the lattice fringes changed from random orientation to a clearer amorphous microcrystal (Figure 2a; Figure S1, Supporting Information). As the pyrolysis temperature further increased to 1300 °C, fine graphite bands were observed, and the coexistence of amorphous zone and local graphitized zone appeared (Figure S1, Supporting Information). Raman spectroscopy confirmed the evolution of the HC crystal phase. The characteristic bands of ≈1355 cm^{-1}(D band) and 1590 cm^{-1}(G band) corresponded to disordered structure and graphite structures, respectively (Figure 2d). With the increase of pyrolysis temperature, both peaks became sharp and a second-order band appeared at ≈2700 cm^{-1}, which was caused by the disappearance

J. Liang
State Key Laboratory of Chemical Resource Engineering
Department of Chemistry
Beijing University of Chemical Technology
Beijing 100029, China

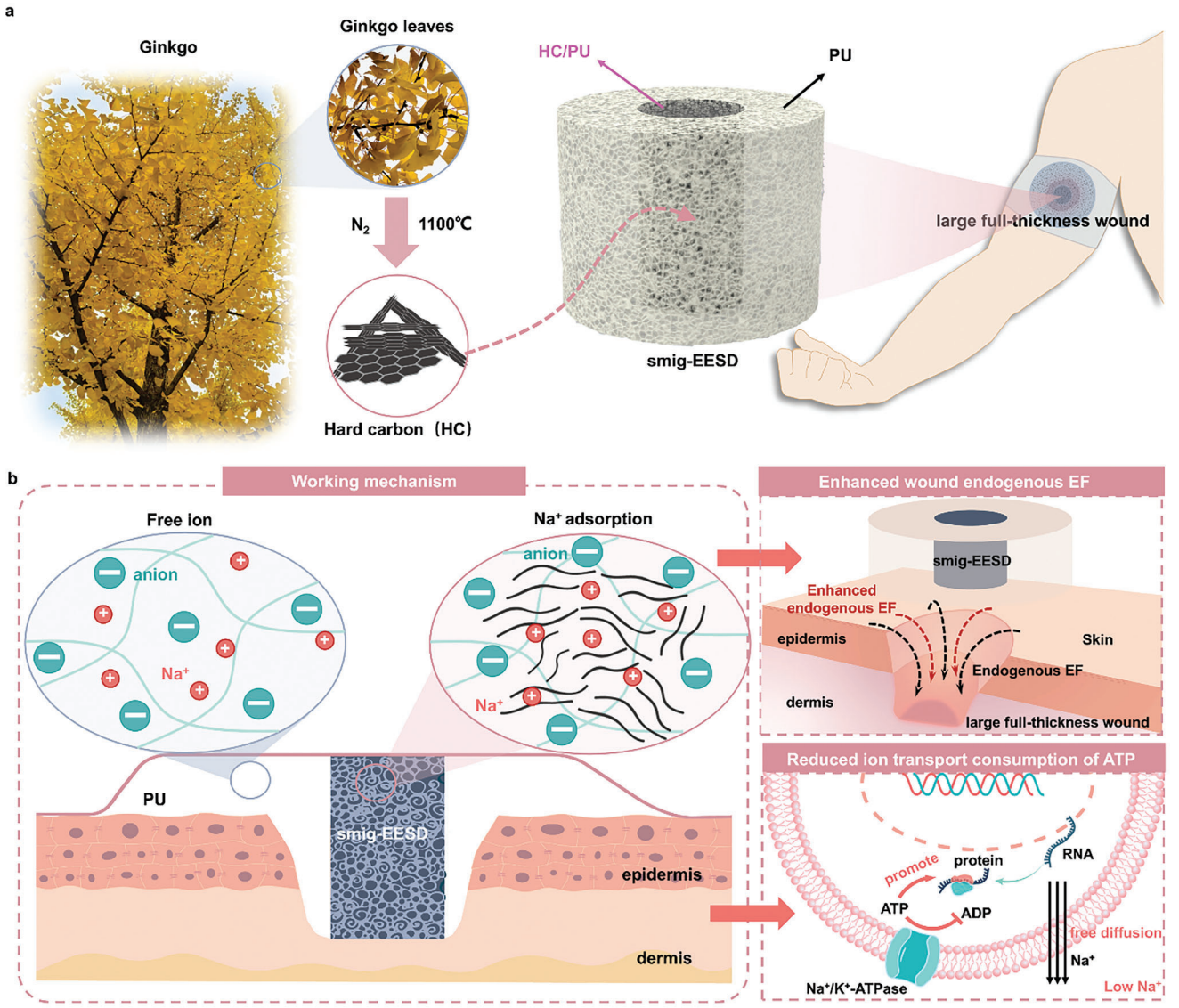

Figure 1. Design and working mechanisms of the smig-EESD for Large-area, full-thickness wound repair. a) The basic structure of smig-EESD: smig-EESD is composed of ordinary PU and PU mixed with HC; HC comes from high-temperature pyrolysis of ginkgo leaves. b) HC/PU in smig-EESD enhanced the wound endogenous electric field by absorbing sodium ions in wound exudate, and saved the active transport of ATP consumed by ions, thus promoting wound repair.

of suspended bonds and the formation of curved graphite layers. The Raman spectral fitting data of HC showed that with the increase of pyrolysis temperature, the peak intensity ratio (I_G/I_D) increased from 0.38 for $HC_{900\,°C}$ to 0.76 for $HC_{1300\,°C}$, indicating that the order degree of carbon materials was gradually increasing (Figure 2d; Figure S3, Supporting Information). XRD spectrum further confirmed that HC prepared by pyrolysis at 900, 1100, and 1300 °C all showed a wide peak at ≈23°, corresponding to the (002) diffraction peak of graphite, which is a characteristic of typical amorphous structure (Figure 2b; Figure S2, Supporting Information). Among them, the (002) peaks of carbon pyrolyzed at 1100 and 1300 °C were asymmetrical, consisting of a sharp peak and a broad peak, which indicates the coexistence of graphite and amorphous regions, consistent with the results observed by HRTEM (Figures S1 and S2, Supporting Information). It has been confirmed that the degree of local graphitization controlled by pyrolysis temperature is the key to controlling the sodium storage performance of carbon materials.[14] To further quantify the changes in the microcrystalline phase with pyrolysis temperature, the carbon (002) peak was simulated through the profile-fitting process (Figure S2 and Table S1, Supporting Information). In Figure S2 (Supporting Information), each part of the fitted peak corresponded to one carbon crystalline phase and is used to calculate the d-spacing. It has been reported that the "pseudo-graphitic" amorphous carbon with d-spacing of 0.36–0.40 nm is relatively favorable for the Na^+ insertion/extraction.[12] The results showed that the proportion of pseudo-graphitic phase at 900, 1100, and 1300 °C were 52.38%, 62.10%, and 82.68%,

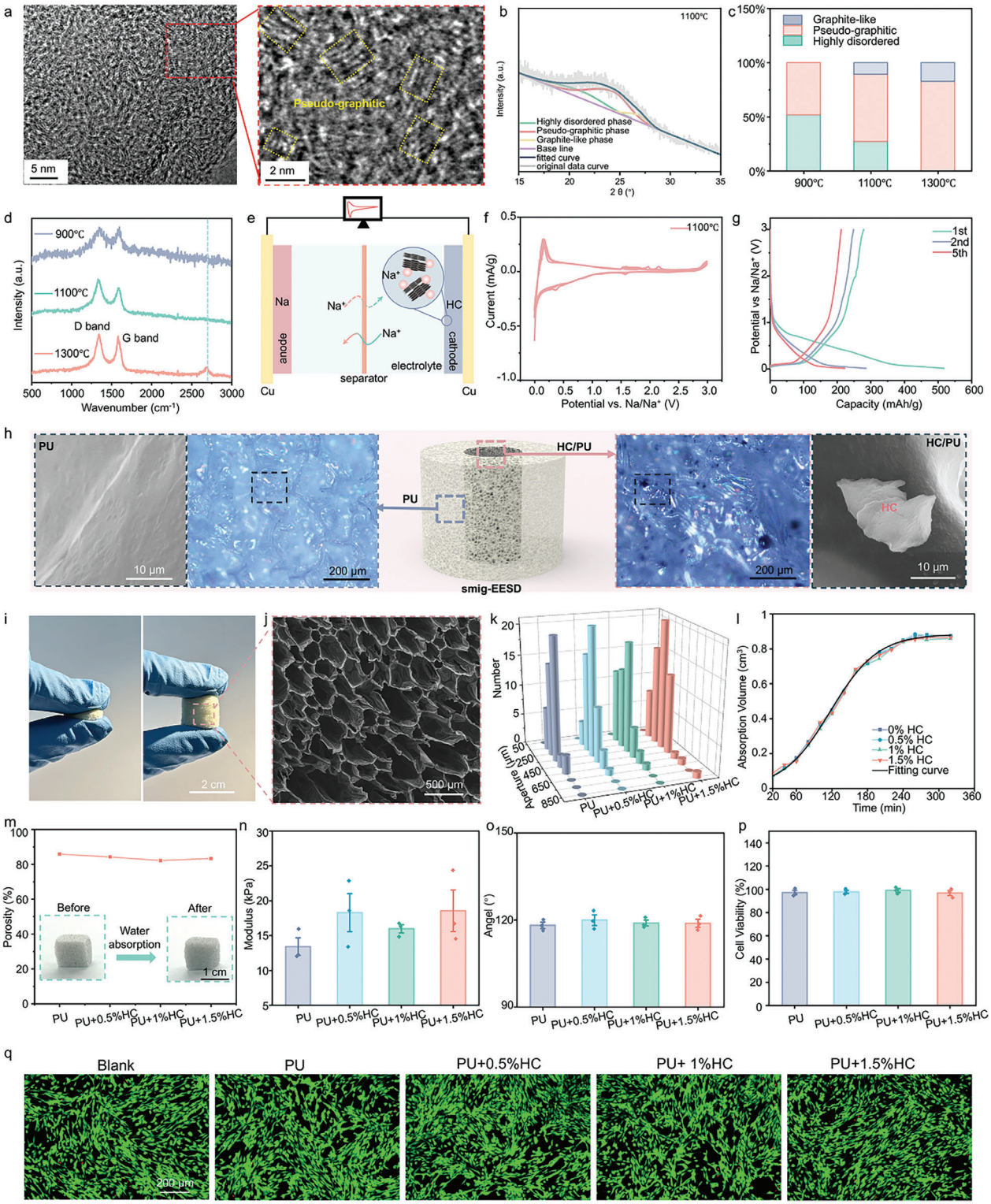

Figure 2. Performance characterization of HC and smig-EESD. a) TEM images of HC. b) XRD patterns and fitting curves of HC at 1100 °C pyrolysis temperature. c) The microstructure evolution of HC samples from a highly disordered state to a pseudo-graphitic state and graphite-like state. d) Raman spectra of HC. Dotted green line is second-order band. e) Schematic diagram of sodium storage performance of HC tested by electrochemical method. f) Cyclic voltammograms of the initial three cycles of the HC samples at 0.1 mV s^{-1}. g) Galvanostatic charge-discharge tests of HC. h) SEM and bright field photos of smig-EESD. i) Real product photo of smig-EESD. j) The porous structure of smig-EESD demonstrated by SEM. k–q) Performance characterization of smig-EESD Aperture distribution (h); water absorption rate (l); water absorption (m); Contact Angle test (n); Young's modulus (o); biocompatibility (p and q). $n \geq 3$ independent samples. Data are presented as mean ± S.E.M.

respectively. Although the pseudo-graphite phase ratio of HC prepared at 1300 °C was comparable to that of HC prepared at 1100 °C, its graphite-like phase ratio (17.32%) was much higher than that of HC prepared at 1100 °C (10.75%). A high proportion of graphite-like phase is unfavorable for Na^+ storage because its d_{002} is lower than 0.36 nm, making it impossible for Na^+ to be inserted.

In order to further determine the pyrolysis temperature of HC with optimal sodium storage performance, HC pyrolyzed at different temperatures was used as cathode and assembled with sodium electrode anode to form a sodium-ion battery (Figure 2e). Since sodium-ion batteries are charged and discharged by the reversible insertion of Na^+ between the positive and negative electrodes, the sodium-ion battery with the largest specific capacity and REDOX peak has the highest sodium storage performance of the HC in the positive electrode. Cyclic voltammetry (CV) between 0.001 and 3.0 V versus Na/Na^+ were carried out to study the electrochemical sodium storage behavior of HC (Figure 2f; Figure S4, Supporting Information). The CV curve showed that the sodium-ion battery prepared by HC pyrolyzed at 900 °C had a weak REDOX peak, while the HC pyrolyzed at 1100 °C and 1300 °C could make the sodium-ion battery have a high and narrow REDOX peak. Galvanostatic charge-discharge tests were performed between 0.001 and 3.0 V versus Na/Na^+ to further determine the pyrolysis temperature of HC with the best sodium storage properties (Figure 2g; Figure S5, Supporting Information). The results showed that HC pyrolyzed at 900, 1100, and 1300 °C all had obvious slope region (> 0.1 V), among which the slope region of $HC_{1100\,°C}$ possessed the largest capacity. A large number of studies have confirmed that the slope region is positively correlated with the defects of HC, and Na^+ is mainly adsorbed on the surface and edge defects of carbon.[15] Therefore, in theory, HC pyrolyzed at 1100 °C could store Na^+ most efficiently through adsorption.

In smig-EESD, the distribution of HC in PU dressing was not uniform: in the middle of smig-EESD covering the center of the wound was the HC/PU dressing that absorbs Na^+ and enhances the wound endogenous EF, and the surrounding area was the PU dressing that supports and protects the wound (Figure 1). The PU dressing was prepared by one-stage process, that is, polyether polyols and various surfactants were mixed and reacted with isocyanate, and then matured at 80 °C to form a porous, sponge-like PU dressing (Figure S6, Supporting Information). HC/PU dressing could be fabricated by adding HC powder during the preparation of PU. The Fourier Transform Infrared spectrum (FT-IR) showed that the absorption peak of HC/PU at ≈3320 cm^{-1} was attributed to the stretching vibration of -NH, and the absorption peak at ≈1716 cm^{-1} represented the stretching vibration of the C═O, confirming that the main component of the synthesized porous dressing was PU (Figure S7, Supporting Information). The optical microscope images showed that HC was evenly distributed in the PU sponge. SEM and EDS images also confirmed that the falke HC was distributed in the pore structure of PU sponge, which is the key for HC/PU dressing to adsorb Na^+ in exudate (Figure 2h; Figures S8 and S9, Supporting Information). As the HC incorporation increased, the HC in HC/PU observed under an optical microscope increased significantly, and the HC in HC/PU could be firmly bound by the PU skeleton and not fall out of the dressing (Figure S8, Supporting Information); however, once the HC incorporation exceeded 2%, HC agglomerated in the PU matrix and is deposited in large quantities at the bottom of the mold.

As a wound dressing, smig-EESD needs to have a flexible porous structure, sufficient exudate absorption capacity, a Young's modulus that matches the skin modulus, hydrophobic properties that prevent tissue cell adhesion, and good biocompatibility.[16] The SEM images showed that HC/PU possessed interconnected porous structure, and its pore size was not affected by HC content (Figure 2i–k). The absorptive capacity of exudate is a necessary property of wound dressing. We tested the water absorption performance of 1 cm^3 PU and HC/PU with different HC content (Figure 2l,m), and found that the water absorption rate of HC/PU was not affected by the HC content. Both PU and HC/PU could absorb ≈85% of the dressing volume, and there was no significant change in the dressing volume before and after water absorption (Figure 2m). In terms of mechanical properties, the modulus of the porous PU dressing was ≈13 kPa, which matched that of the skin (6–222 kPa).[17] The modulus of HC/PU (13–25 kPa) increased after the incorporation of HC, but there was no statistical difference in the Young's modulus of HC/PU with different HC contents, all within the appropriate range of the skin modulus (Figure 2n). The contact angles of PU and HC/PU were much greater than 90°, which means that PU and HC/PU were hydrophobic and possessed the potential to prevent tissue adhesion. In order to better confirm that HC/PU can prevent adhesion of tissues, we cultured HaCaT cells (epidermal cells) and NIH3T3 cells (fibroblasts) on the surface of HC/PU for 2 days and observed the attachment of cells on the dressing surface by SEM. The results showed that almost no cells were attached to the surface of HC/PU, indicating that the dressing has the ability to prevent tissue adhesion (Figure 2o; Figure S10, Supporting Information). Biocompatibility determines whether a dressing could be applied to the human skin. The CCK-8 and cell viability/cytotoxicity assay images showed that PU and HC/PU had no effect on the activity and proliferation of NIH3T3 cells, indicating that both PU and HC/PU were excellent biocompatible wound dressings for skin wounds (Figure 2p,q; Figure S11, Supporting Information).

2.2. smig-EESD Selectively Absorbed Na^+ in the Wound Center to Expand the Cation Concentration Gradient, thereby Enhancing the Wound Endogenous EF

The unique structure of smig-EESD was designed based on a deep understanding of the mechanism of endogenous EF formation in wounds. When using smig-EESD to treat wounds, the HC/PU area in the middle of the smig-EESD needs to be fixed in the center of the wound, while the PU part covers the peripheral part of the wound and a part of the normal skin. In theory, smig-EESD could self-manipulate the endogenous ionic gradient by absorbing Na^+ ions in the center of the wound, ultimately enhancing the endogenous EF, which provides a novel endogenic electrical stimulation treatment strategy that is completely different from the any existing exogenous electrical stimulation mode (**Figure 3**a–c).

The distribution of ion channels on the epidermal cell membrane is uneven: the chloride channel distributed at the top of

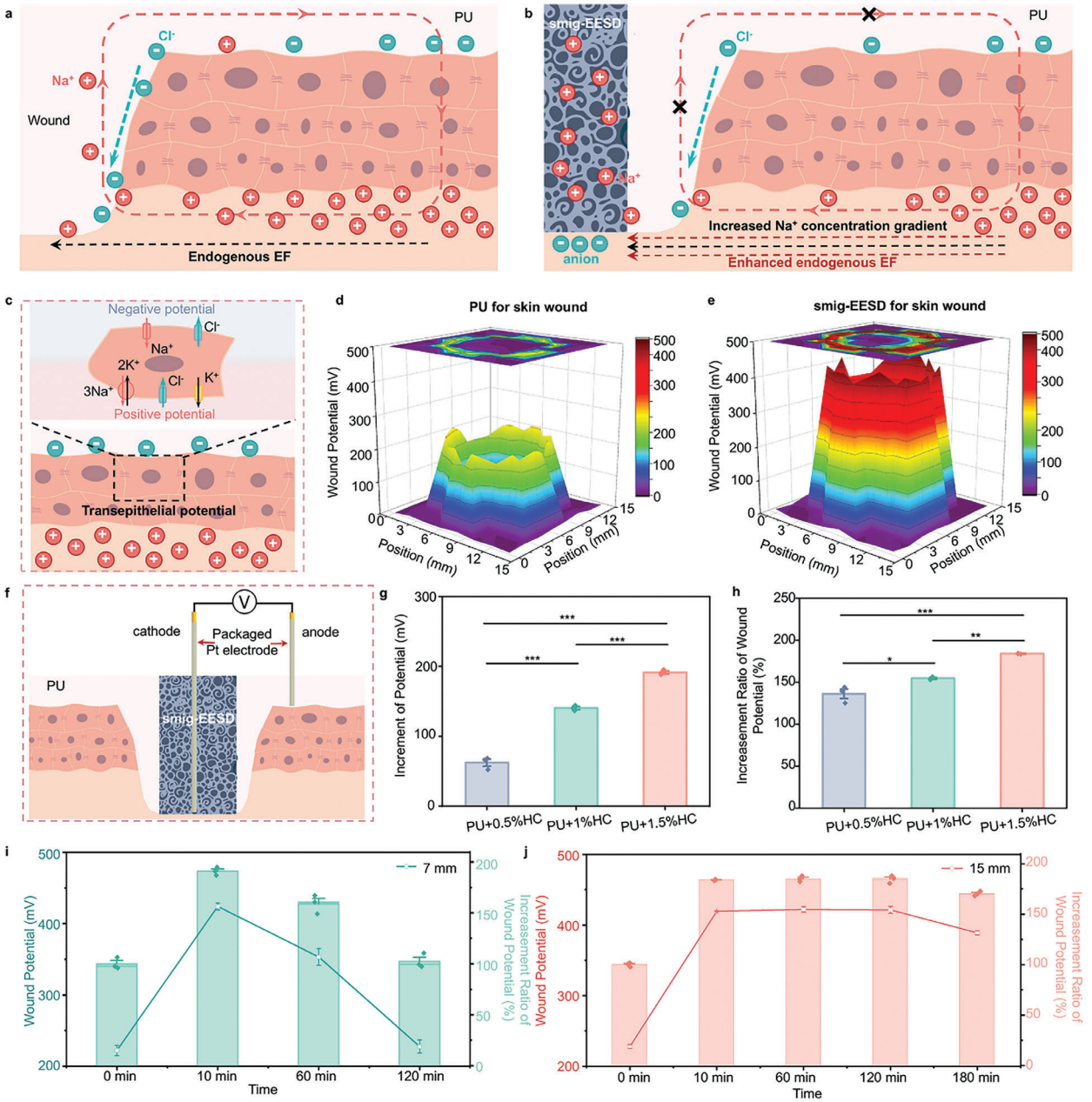

Figure 3. Effect of the smig-EESD on wound potential. a) Effect of PU dressing on wound potential. b) Effect of smig-EESD dressing on wound potential. c) Mechanism of skin TEP generation. d) 3D profile of the wound potential in the PU group. e) 3D profile of the wound potential in the smig-EESD (1.5% HC) group. f) Schematic diagram of measuring wound potential. g) Increment of potential with different carbon content. h) Increasement ratio of wound potential with different carbon content. i) Effect of the smig-EESD with height of 7 mm on wound potential. j) Effect of the smig-EESD with height of 15 mm on wound potential. $n \geq 3$ independent samples. Data are presented as mean ± S.E.M.

the cell transports one Cl^- ion to the extracellular matrix at a time, while the sodium pump at the bottom of the cell pumps three Na^+ ions out to the extracellular matrix (Figure 3c). However, due to the tight connections between epidermal cells, it is difficult for Cl^- accumulated in the upper layer and Na^+ accumulated in the lower layer to achieve charge balance through the intercellular space, thus forming a transepithelial potential (TEP) on the surface of normal skin.[4,18] Once the integrity of the skin is damaged, the TEP is short-circuited and formed ionic flux loop of Na+:[6] the destruction of tight junctions at the center of the wound causes the overflow of sodium ions from the lower layer and neutralization with the chloride ions from the upper layer, forming a zero potential point; while the sodium ion gradient difference at the distal end of the wound is not affected; therefore, an endogenous EF is formed from the wound periphery to the wound center. In normal mouse wounds, the potential is distributed in a volcano-shaped pattern, that is, the potential around the wound is high and the potential in the wound center

is low. A mouse full-layer skin wound model (circular defect with a diameter of 10 mm) was established, and measurements confirmed that there was a potential difference of ≈230 mV from the wound periphery to the center (Figure 3a,d). Na^+ flow and Cl^- flow not only play an important role in the formation and maintenance of the wound endogenous EF, but also the main electrolytes in the exudate of skin wounds. smig-EESD with the specific adsorption performance of Na^+ could interfere with the flow of Na^+ in the wound: smig-EESD directly captured the sodium ions flowing from the epidermal layer base to the top of the wound edge, forming a larger Na^+ gradient; on the other hand, smig-EESD did not affect the flow of Cl^- in the opposite direction of the Na^+ flow, so that a large amount of Cl^- that should had been neutralized stayed in the center of the wound; ultimately leading to an increase in the intensity of the endogenous EF directed from the wound edge to the wound center (Figure 3b). Under the intervention of smig-EESD, the wound potential difference could be increased to and maintained at ≈415 mV (Figure 3e).

To further prove that the enhancement of endogenous EF in the wound surface was related to the selective adsorption of Na^+ (Figure S12, Supporting Information), smig-EESD was immersed in simulated body fluid and the adsorbed Na^+ content was detected. After immersion for 3 h, the Na^+ content in the solution was significantly reduced using a Na^+ selective electrode (decreased by ≈5.3 mmol L^{-1}). The effects of HC/PU with different HC contents on the wound endogenous EF were further investigated, and the changes in wound potential before and after different dressing treatments were recorded (Figure 3f). Figure 3g showed the wound potential measured after dressing treatment increased with higher HC content, and 1.5% HC could increase the wound potential by 83.9% compared with the initial potential (Figure 3h; Figure S13, Supporting Information). Subsequently, we applied different volumes (same cross sectional area but different thickness) of smig-EESD with 1.5% HC content to mouse wounds and monitored the real-time change of wound potential. Small volume smig-EESD (7 mm thickness) could increase the wound potential to ≈424 mV after 10 min, but the enhanced wound potential dropped sharply at 60 min and returned to the initial wound potential at 120 min (Figure 3i; Figure S14, Supporting Information). In contrast, the large volume smig-EESD (15 mm thickness) maintained more than 180% of the initial potential (≈230 mV) within 180 mins, and it did not drop to the initial wound potential until 240 mins (Figure 3j; Figure S15, Supporting Information). The large-volume and high-HC content smig-EESD was significantly superior to the small-volume and low-HC content smig-EESD in terms of the average increase in wound potential and the duration of maintaining the enhanced endogenous EF, better meeting the needs of wound electrical stimulation therapy (the duration of clinical electrical stimulation is usually from 0.5 to 2 h).[19] Therefore, we selected a smig-EESD with a thickness of 15 mm and HC content of 1.5% for subsequent experiments.

2.3. smig-EESD Effectively Decreased Inflammatory Infiltration, Accelerated Wound Repair, and Reduced Scar Formation

The wound theoretical model and in vivo animal experiments confirmed that smig-EESD could enhance the wound endogenous EF by specifically adsorbing Na^+ ions in the wound center. To further evaluate the therapeutic effect of endogenic electrical stimulation generated by smig-EESD on full-layer wounds in vivo, clinical large-area wound model with exudate was established in mice (a circular defect with a diameter of 10 mm was cut out on the mouse skin surface, and 3 mL of PBS (theoretical exudate loss) was slowly added to simulate the exudate). The wound self-healing model covered only with PU dressing was defined as the Blank group (**Figure** 4a), and the C/PU dressing prepared by incorporating PU with amorphous carbon with almost no sodium storage performance was used as the control group to exclude the effect of the chemical composition of carbon materials on wound healing (Figure 4a; Figure S16, Supporting Information). In clinical practice, large-area wounds have a large amount of exudation in the first three days, so the wounds were first intervened with each group of dressings (Blank group, C/PU group, smig-EESD group) for three days, and then all groups were replaced with PU dressings to protect the wounds until the wounds closed (Figure 4b). In theory, the enhanced endogenous electric field of the wound caused by the specific adsorption of Na^+ by smig-EESD can trigger the electrotactic response of epithelial cells, thereby promoting wound healing. According to surgical photos and wound area analysis, smig-EESD significantly promoted wound healing and reduced scar formation (Figure 4c). In the early stage of proliferation (day 3), the healing area of the smig-EESD group was 49.12%, and its healing speed was much higher than that of the other groups, which was 2.69 and 2.83 times that of the C/PU group (18.24%) and the Blank PU group (17.33%), respectively (Figure 4c,d; Figure S17, Supporting Information). On the 6^{th} day of wound healing, most wounds in the smig-EESD group were successfully repaired (83.1%), which was significantly higher than those in the C/PU group (66.54%) and the Blank group (65.8%) (Figure 4d). On the 11^{th} day, the smig-EESD group was almost completely healed, while less than 10% of the wounds in both the C/PU group and the blank group were not completely healed (Figure 4d). In the subsequent remodeling process, the scar area of the C/PU group and the Blank group was ≈15 mm^2 on the 30^{th} day, however, the smig-EESD group formed a very small scar on the skin surface, which was only 1/3 of the Blank group (Figure 4e). In addition, smig-EESD has been shown to have the potential to promote chronic wound healing in diabetic wounds (Figure S18, Supporting Information).

The wound healing process is divided into three important phases: inflammation, proliferation, and remodeling.[20] Since the duration of the inflammatory period determines when proliferation begins, we focused on the pathological sections of wound tissue within three days of treatment and used H&E staining to measure the density of inflammatory cells at the wound margin (Figure 4f–j). Neutrophils are important cells in the acute inflammatory stage. On the first day of treatment, the density of neutrophils in the three groups was similar; on the second day, the neutrophils in the smig-EESD group showed a downward trend, while the neutrophil density of the C/PU group and the Blank group continued to increase (Figure 4f,h). When entering the proliferation phase on the third day, the neutrophil density decreased slightly in the C/PU and Blank groups, while only a small number of neutrophils were observed in the smig-EESD group. These results confirmed that the smig-EESD facilitated the control of inflammation caused by acute injury. Since the number

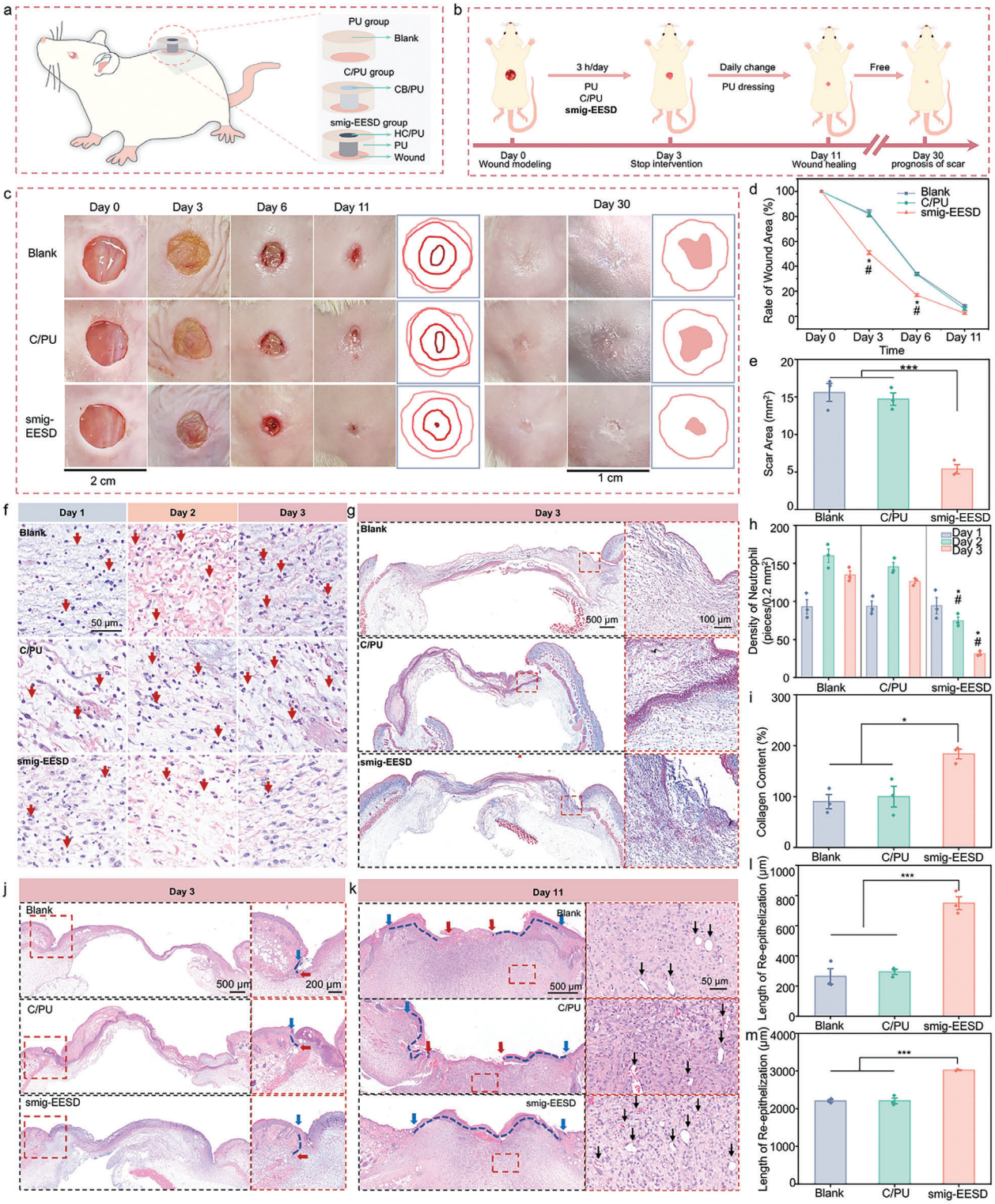

Figure 4. Therapeutic efficacies of the smig-EESD on wound repair. a) Dressing composition and treatment mode in different groups. b) Treatment schedule. c) Photographs of wound and wound contour under different treatment modes. d) Rate of wound area. e) Scar area (Day 30). * and # indicate the significant differences ($p < 0.05$) between group smig-EESD and Blank, C/PU, respectively. f) Distribution of neutrophils in wound tissue (Day 1, 2, and 3). Neutrophils (lobulated nucleus, ≈11 um), red arrow. g) Masson staining of wound granulation tissue. h) Density of neutrophils. * and # indicate the significant differences ($p < 0.05$) between group smig-EESD and Blank, C/PU, respectively. i) Collagen content of granulation tissue. j) H&E staining of wound tissue (Day 3). k) H&E staining of wound tissue (Day 11). New vessels in the granulation tissue, black arrow. l) Length of re-epithelization in different groups (Day 3). m) Length of re-epithelization in different groups (Day 11). $n \geq 3$ independent samples. Data are presented as mean ± S.E.M.

of phagocytes in the three groups was similar on the first day of treatment, we speculated that smig-EESD did not affect the function of innate immune cells to clear dead cells and cell debris during the inflammatory phase of the wound, but it would shorten the inflammatory phase and make it enter the proliferation phase more quickly. The formation and re-epithelialization of new granulation tissue are the main features of the proliferative phase, which is the key stage of wound repair. The regenerated granulation tissue is mainly composed of proliferating fibroblasts and the collagen secreted by them, so the Masson staining was used to mark collagen (Figure 4g). The statistical results showed that smig-EESD could promote wounds to produce more collagen, thereby allowing new granulation tissue to grow faster (Figure 4i). Re-epithelialization is the essential feature of intact epidermal barrier recovery (Figure 4j–m). As shown in Figure 4j, smig-EESD showed excellent ability to promote wound re-epithelialization while accelerating wound closure, and increased the length of re-epithelialization without affecting the thickness of re-epithelialization (Figure 4l; Figure S19, Supporting Information). When the wound of the smig-EESD group formed a complete epidermis (Day 11), the re-epithelialization length in the C/PU group and the Blank group was 73.11% and 73.02% of that in the smig-EESD group, respectively; while the thickness of the newly formed epidermis between the groups was not significantly different (Figure 4k,m; Figure S20, Supporting Information). At the same time, H&E staining images showed that compared with the C/PU and the Blank groups, there were a large number of new blood vessels in the newly formed granulation tissue of the smig-EESD group (Figure S20, Supporting Information). The above results indicated that smig-EESD significantly accelerated the entire development process of wound repair through endogenic electrical stimulation without affecting the inherent functions of each stage of wound healing process, thereby achieving rapid repair of skin wounds.

2.4. The Self-Manipulation of Ion Gradients by smig-EESD Intervened with ATP-Mediated Ion Transport Process by Altering the Transport Mode of Na^+ from the Intracellular to the Extracellular Matrix

To deeply understand the mechanism of smig-EESD promoting wound repair, transcriptome sequencing was performed on the wound tissues of Blank group and smig-EESD group on the 6th Day. The results of volcanic map and heat map showed that compare with the Blank group, the expression of a large number of genes changed significantly after smig-EESD treatment (**Figure** 5a,b). More than 2000 differentially expressed genes were enriched by GO, confirming that smig-EESD significantly up-regulated the expression of genes involved in wound healing, skin development, epidermal cell proliferation, migration, differentiation, keratinization, and fibroblast proliferation (Figure 5c). In addition, smig-EESD also up-regulated genes related to hair follicle regeneration and vascularization, suggesting that smig-EESD possessed great potential in promoting hair follicle regeneration and vascularization in wound tissue (Figure 5d; Figure S21, Supporting Information).

Interestingly, after smig-EESD treatment, genes related to Na^+ active transport were significantly down-regulated, especially the expression of ATP-driven sodium-potassium pumps, such as ATP1b1 and ATP1b2 (Figure 5e–g). ATP1b1 and ATP1b2 are important components of the β-subunit of Na^+/K^+-ATPase.[21] Downregulation of the β-subunit expression will affect the structural and functional maturation of Na^+/K^+-ATPase, ultimately leading to the decline of the activity of Na^+/K^+-ATPase (Figure 5e). It is worth noting that although processes associated with ion transport and ATPase complex were inhibited at the RNA level, biological processes related to protein synthesis were up-regulated, accompanied by downregulation of gene transcription involved in protein degradation (Figure 5g). This result revealed that smig-EESD intervened in the cells' transmembrane ion transport process through precise sodium ion manipulation, ultimately triggering a series of biochemical chain reactions related to material and energy metabolism. For normal cells, the Na^+ concentration in the extracellular matrix is higher than that in the cytoplasm. To maintain the osmotic pressure inside and outside the cell, the cell needs to transport Na^+ from the cell to the extracellular matrix against the concentration gradient through the sodium-potassium pump, which is accompanied by the consumption of ATP. After receiving smig-EESD treatment, the Na+ in the extracellular matrix is bound by the dressing, thereby reversing the concentration gradient of Na ions inside and outside the cell. The transport of Na^+ in the cell no longer depends on the sodium-potassium pump, but can directly diffuse into the extracellular matrix along the concentration gradient, which undoubtedly saves the basic consumption of ATP. We further analyzed the genes involved in both active Na^+ transport and ATP metabolism based on string diagram, and identified that the downregulation of ATP1b1 gene was associated with the occurrence of both processes (Figure 5i). Low Na^+ environment might decrease Na^+, K^+ -ATPase activity unrelated to its inhibitory effect, but it might be a homeostasis mechanism to maintain Na^+ balance in animals.[22] Based on the transcriptome analysis, it is reasonable to speculate that the basal ATP consumption saved by altering Na^+ transport patterns might be used to promote protein synthesis for tissue repair. To confirm the above view, HaCaT cells were cultured in a medium containing HC, the core component of smig-EESD, to observe whether selective adsorption of Na^+ would interfere with cell behavior. Both fluorescence quantitative PCR (qPCR) and immunofluorescence staining confirmed that HC could down-regulate the expression of ATP1b1, but up-regulate the expression of Ki67, a typical cell proliferation indicator (Figure 5j–l; Figures S22 and S23, Supporting Information) and the ATP content in HaCaT cells (Figure S24, Supporting Information). This result confirmed our speculation that HC in smig-EESD might change the active transport of Na^+ by the sodium-potassium pump to passive diffusion, thereby reducing ATP consumption (Figure 5m,n). The saved ATP could be used for protein synthesis related to cell proliferation, and ultimately promoted tissue repair.

2.5. smig-EESD Regulated Innate and Adaptive Immune Responses by Promoting Paracrine Secretion of Histiocytes

During tissue repair, tissue cells regulate the tissue immune microenvironment by paracrine secretion of various cytokines, thereby further promoting cell proliferation and differentiation.

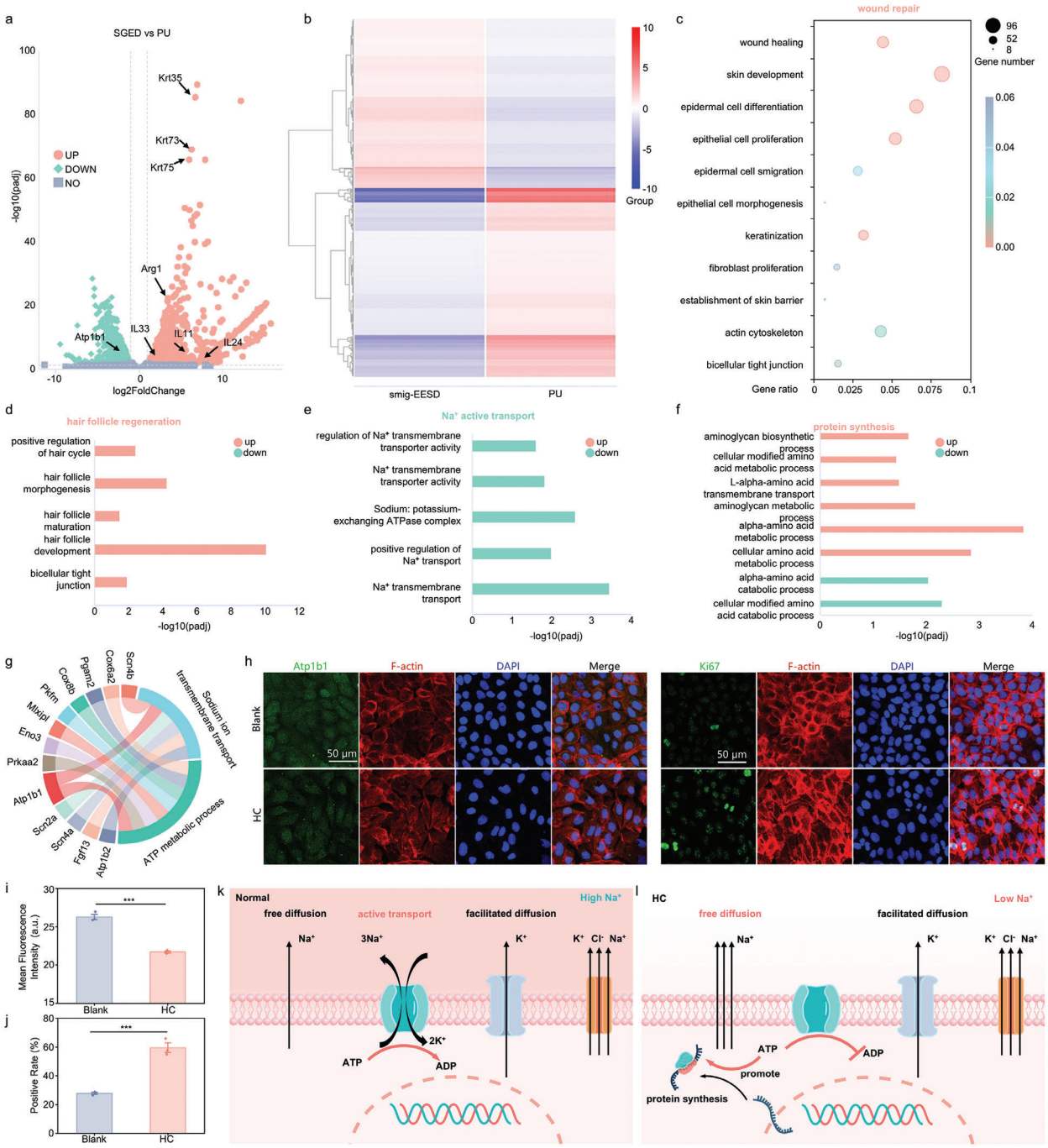

Figure 5. Exploration of gene expression patterns and functional enrichment analysis. a) Volcano plot of differential expression genes. Keratinization: Krt35, Krt73, Krt75; M2 macrophage: Arg1; Na^+/K^+-ATPase: Atp1b1; cytokines: IL11, IL24, IL33. b) Heatmap of differential expression genes. c–f) GO enrichment analysis. g) Chordal graph of differential expression genes. h) Immunofluorescent staining of HaCaT cells. i) Mean fluorescence intensity of Atp1b1. j) Positive rate of Ki67. k) The process of sodium ion transport in cells under physiological conditions. l) The process of sodium ion transport in cells occurs when the extracellular sodium ion concentration is low. $n \geq 3$ independent samples. Data are presented as mean ± S.E.M.

After enriching all differentially expressed genes by RNA sequencing, we found that smig-EESD up-regulated genes related to protein secretion and cytokine activity, especially for the gene expression of IL11, IL24, and IL33 (**Figure** 6a,b). In our previous work, it has been confirmed that enhanced endogenous electric fields in wounds can promote M2 polarization of macrophages[18] In the treatment of smig-EESD, in addition to the polarization- inducing effect of endogenous electrical stimulation, we also found that IL24 secreted by epidermal cells and IL11 secreted by fibroblasts were also upregulated, synergistically promoting the polarization of M2 macrophages.[23] In addition to regulating the phenotypic transformation of innate immune cells to inhibit

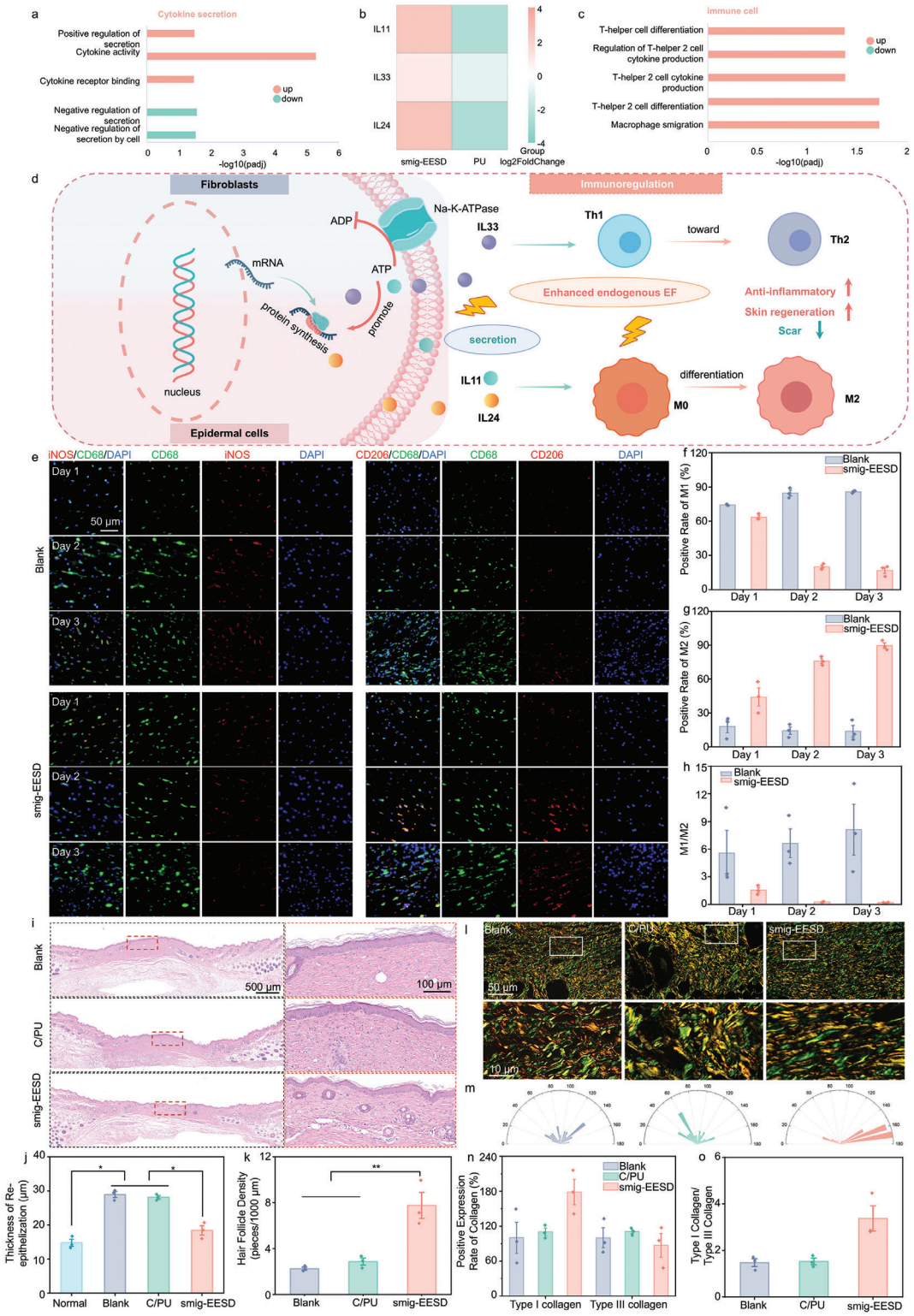

Figure 6. Effects of smig-EESD on immune cell and tissue remodeling. a) GO enrichment analysis of cytokines secretion. b) Expression of cytokines secretion. c) GO enrichment analysis of Th2 and macrophages. d) Schematic diagram of smig-EESD regulating immunity. e) Immunofluorescent staining of wound tissue. f) Positive rate of M1. g) Positive rate of M2. h) The ratio of M1 to M2. i) H&E staining of wounds in different groups (Day 30). j) Thickness of re-epithelialized center in different groups. k) Density of hair follicle in H&E staining. l) Sirius red staining in the center of the repaired tissue in different groups (Day 30). m) Relative angle of collagen in different groups. n) Relative content of collagen compared with the PU group. o) The ratio of type I collagen to type III collagen $n \geq 3$ independent samples. Data are presented as mean ± S.E.M.

inflammation and promote tissue repair, smig-EESD further intervened in the adaptive immune response. Transcriptome analysis showed that smig-EESD upregulated the secretion of IL33 by fibroblasts.[24] Cell experiments confirmed that the secretion of IL33 in fibroblasts were upregulated in a simulated endogenous electric field environment. IL33 can act on the ST2 receptor of helper T cells (Th), inducing the Th1/Th2 balance to shift toward Th2 (Figure 6c; Figure S25, Supporting Information).[25] With increased Th2 differentiation, the proliferation of Th1 cells was inhibited, thereby reducing the secretion of pro-inflammatory cytokines.[26] In conclusion, smig-EESD provided an immune microenvironment conducive to tissue repair, which might be attributed to the characteristics of endogenic electrical stimulation and involvement in energy metabolism (Figure 6d).

Immunofluorescence staining provided intuitive evidence that smig-EESD promoted the transition of macrophages from proinflammatory M1 phenotype to reparative M2 phenotype, which is a typical sign of the transformation of wounds from inflammatory phase to proliferative phase.[27] M1 macrophages were labeled with iNOS and CD68, and M2 macrophages were labeled with CD206 and CD68 by immunofluorescence staining (Figure 6e–h; Figures S26–S28, Supporting Information). On the 1st day of treatment, the total number of macrophages (CD68-labeled) in smig-EESD group was significantly higher than that in the Blank group and C/PU group. There was no difference in the positive rate of M1 macrophages among the three groups, but the number of M2 macrophage maker-positive cells in the smig-EESD group was higher than that in the Blank and C/PU groups (Figure 6e–h; Figures S26–S28, Supporting Information). These results suggested that smig-EESD might accelerate the recruitment of macrophages in the early stage of wound inflammation, and change the ratio of M1/M2 by increasing the number of M2 macrophages, which was beneficial for the wound tissue to reduce the inflammatory state and transform to the repair process. In the subsequent two days of treatment, there was no difference in the total amount of macrophages among the three groups. On 3rd day, the proportion of M2 macrophages in the Blank and C/PU groups remained below 20% while the proportion of M2 macrophages in the smig-EESD group increased to ≈90%. In addition, statistics of macrophages in the regenerated granulation tissue on the 3rd day showed that the number of macrophages in the new granulation tissue of smig-EESD group was significantly higher than that of the Blank group (1.38 times) and the C/PU group (1.44 times); and M2 macrophages were the mainstream in the smig-EESD group, accounting for up to 72% (Figure S27, Supporting Information). It can be seen that smig-EESD accelerated the polarization of M2 macrophages, causing the wound to rapidly transition from the inflammatory phase to the proliferation phase, thereby promoting wound repair.

2.6. smig-EESD Advanced the Remodeling Phase of Wound Repair, Reduced the Formation of Scars, and Improved the Skin Healing Quality

The healing of full-thickness skin wounds is often imperfect, and the repair process may lead to hypertrophic scars and loss of skin appendages, which not only affects aesthetics but also cause itching, pain and dysfunction.[28] There is increasing evidence that wound inflammation is directly related to poor healing and scar formation. M2 polarization of macrophages in the early stage of wound healing can improve the speed of wound healing and the quality of wound repair, while inhibiting scar formation.[29]

Transcriptome results suggested that smig-EESD possessed the potential to promote the regeneration of hair follicles in newborn skin tissue. H&E staining of skin tissue on the 30th day after treatment showed that the average thickness of the newly formed epidermis during the remodeling phase in smig-EESD group was 18.4 μm, which was significantly lower than that in the Blank group (28.9 μm) and C/PU group (28.1 μm), and closer to the normal skin tissue thickness (≈14.8 μm). Moreover, in the smig-EESD group, a large number of new hair follicles were also found in the center of the newly formed epidermis, and their density was significantly higher than that in the Blank group (3.45 times) and the C/PU group (2.71 times) (Figure 6i–k). These observations confirmed that smig-EESD accelerated the maturation of epithelial tissue and appendages during the remodeling phase.

In addition to epithelial maturation, granulation tissue remodeling is the most critical step in the formation of new dermis.[30] Disordered extracellular matrix in granulation tissue may eventually lead to scar formation. During the remodeling process, the new granulation tissue, which is mainly composed of type III collagen, is partially replaced by type I collagen with better stability and elastic tension to enhance the strength of repaired skin.[31] Sirius red staining distinguishes type I collagen from type III collagen under polarized light (Figure 6l–o). In normal skin, the ratio of type I collagen to type III collagen (I/III) is maintained at ≈4:1. The content of type I collagen in the repaired tissue of the smig-EESD group was higher than that of the Blank and C/PU groups, while the content of type III collagen in the three groups was comparable; therefore, the ratio of type I/III collagen in the smig-EESD group was 3.37:1, which was more similar to the dermis of normal skin than that of the new dermis of the Blank group (1.48:1) and the C/PU group (1.53:1) (Figure 6o). Besides, the directionality of collagen arrangement also plays an important role in scar formation, and disordered collagen arrangement will lead to fragile mechanical properties of the regenerated dermis.[32] Compared with the random arrangement of collagen in the Blank group and the C/PU group, the arrangement of collagen in the smig-EESD group showed obvious directionality (Figure 6m). These results suggested that smig-EESD effectively promoted orderly remodeling of the extracellular matrix, thereby improving the quality of repaired skin tissue and inhibiting scar formation.

3. Conclusion

Based on the understanding of cation flow that forms wound endogenous EF, we established a manipulable cation concentration gradient-based endogenic electrical stimulation dressing (smig-EESD) by selectively absorbing Na^+ in exudate, and its strengthened wound EF accelerated the entire wound repair process. Animal studies highlighted the superior efficacy of smig-EESD in the treatment of heavily exuding skin wounds: endogenic electrical stimulation shortened the inflammatory phase of the wound, promoted the inflammatory/proliferative transition, accelerated the re-epithelialization process during the

proliferation phase, and facilitated wound closure. smig-EESD also converted the cell transmembrane transport of Na^+ from active transport dependent on Na^+/K^+-ATPase against the concentration gradient to passive diffusion along the concentration gradient by adsorbing Na^+ in the extracellular matrix. The ATP saved by Na^+ transmembrane transport was used to facilitate protein synthesis in tissue repair. smig-EESD enhanced the secretion of histocytes and immune cells, thereby regulating the innate and adaptive immune responses to inhibit injury-related inflammatory responses. smig-EESD inhibited scar formation while reestablishing skin appendages and extracellular matrix, significantly improving the quality of skin repair and making the repaired skin tissue more mature. The proposed smig-EESD reveals an innovative method of endogenic electrical stimulation. Superior to traditional electrical stimulation strategies, the endogenic electrical stimulation based on smig-EESD does not require electrodes, power supplies, and circuits, and its mechanism of self-manipulating the cation concentration gradient also avoids side effects such as electrochemical reactions and thermal effects. smig-EESD will inspire future research on electrical stimulation therapy and provide new insights for the development of electronic medicine.

4. Experimental Section

Preparation of HC: Hard carbon was obtained from ginkgo biloba leaves. Ginkgo leaves were dried and ground into powder. Ginkgo biloba leaf powder was fired in a tube furnace under N2 (99.999%) atmosphere for 2 h with a heating rate of 5 °C min^{-1} to obtain hard carbon. The hard carbon was ground and purified with 3 M hydrochloric acid (HCl) and deionized water. Dry overnight in a vacuum drying oven at 120 °C. The purified hard carbon was dried overnight in a vacuum drying oven at 120 °C.

Characterization of HC: The morphology of carbon was observed with transmission electron microscope (FEI F20). The carbon material was characterized by X-ray Powder diffractometer (Xpert3 Powder). The scanning parameters were as follows: Angle $2\theta = 5°–50°$, Cu Kα ray was used, tube flow was 40 mA, tube pressure was 40 kV. Raman tests were performed at room temperature with a 532 nm laser as the excitation source on the LabRAM HR Evolution high-resolution confocal Raman microscope. XRD data of carbon obtained at different pyrolysis temperatures were profile-fitting process using jade6 software.

The resulting material powder was mixed with a conductive agent (Super P) and a binder (polyvinylidene fluoride PVDF) at a mass ratio of 8:1:1 to form a uniform slurry. Then, the slurry was evenly coated on the copper foil (99.9% purity, 10 µm thickness) with a scraper on the collector fluid, and then dried in a vacuum oven at 110 °C for 12 h. In the glove box, the completely dried electrode sheet was fabricated into a 12 mm diameter electrode sheet with a chip machine, and then assembled into a CR2032 battery with a sodium sheet (16 mm diameter, 0.5 mm thickness) and a 1 M $NaClO_4$ electrolyte (EC: DEC = 1:1) commercial glass fiber diaphragm (Whatman Company). The electrolyte in the battery was ≈100 µl. During electrochemical testing, the Neware battery test system was used to test battery performance, such as cycle stability and rate performance. Cyclic voltammetry (CV) and Galvanostatic charge–discharge tests was performed using CHI660E Electrochemical workstation (Shanghai Chenhua Instrument Co., LTD.).

Preparation of the Dressing: PU was prepared by a one-step process of medical polyurethane foam dressings. Polyether polyol (PPG, 45 g, YUANYE, S25590), deionized water (5 g), polyethylene polypyrrolidone (PVPP, 0.5 g, Aladdin, A24067) and other additives (anhydrous ethanol 5 g, silicone oil 1.25 g, dibutyltin dilaurate 0.05 ml, triethylamine alcohol 0.105 ml, 1.4-butanediol 0.25 g, glycerol polyoxyethylene ether 5 g; all the reagents came from Aladdin) pour into the container and stir well to obtain the mixture. 4, 4-Diphenylmethane-diisocyanate (MDI, 50 g, Sigma-Aldrich, 33 428) was added to the mixture at 2000 rpm. Stir until the mixture turns milky white (10 s). Pour the mixture into the mold and age for 1 h to produce PU. The preparation of HC/PU required that HC was mixed into the mixture before MDI is added.

PU without HC was synthesized by a one-step method, and then a large piece of PU was cut into hollow cylinders with an inner diameter of 7 mm and an outer diameter of 13 mm using a cutter. Then, a mixed solution of polyether polyol and 4, 4-diphenylmethane-diisocyanate containing HC was rapidly stirred and injected into the hollow cylindrical PU for foaming and ripening, and finally obtaining smig-EESD.

Characterization of the Dressing: Fourier transform-infrared (FT-IR) spectra (VERTEX80v, Bruker) was used to confirm PU synthesis. PU and HC/PU was observed by a cold field emission scanning electron microscope (SEM, SU8020) and metallographic microscope (Sony). The contact Angle was measured by the contact Angle meter (Hokuto, CA500). The mechanical property of PU and HC/PU was measured using a dynamometer (Force Gauge Model, Mark-10, USA). smig-EESD was soaked in 1× phosphate-buffered saline (PBS) and incubated in a shaker at 37 °C (200 rpm min^{-1}) for three days. The drop of HC was observed by microscope.

Cell Culture: NIH3T3 and HaCaT cells were obtained from the Cell Bank of the Chinese Academy of Sciences in Beijing, China. HaCaT cells were cultured in 1640 medium (31 800, Solarbio) containing 10% fetal bovine serum (FBS, Gibco) and 1% penicillin/streptomycin (P1400, Solarbio). NIH3T3 was cultured in DMEM medium with high glucose (11 995, Solarbio) containing 10% fetal bovine serum (FBS, Gibco) and 1% penicillin/streptomycin (P1400, Solarbio). The cell culture condition was humid incubator (CCL-170B-8, ESCO) with 5% CO_2 at 37 °C.

Biocompatibility: NIH3T3 were used for cell viability. The Cell Viability/Cytotoxicity Detection and CCK-8 was used to assess NIH3T3 cell viability. Confocal fluorescence microscope (Leica SP8) was used for obtaining images. The microplate reader (BioRad iMark) was applied to test absorbance.

Cell Adhesion: A circular 1.5% HC/PU dressing with a diameter of 1.5 cm was placed in a 12-well plate, and $1*10^6$ HaCaT and NIH3T3 cells were inoculated on the dressing. After 2 days, the HC/PU dressing inoculated with cells was dehydrated. SEM (SU8020) was used to observe the attachment of cells to the HC/PU surface.

Detection of Sodium Ion Concentration: The formula of the ion selective permeable membrane of the Na^+ sensor was as follows:1 wt.% of 1 sodium ion carrier X; 65.45 wt.% DOS (dioctylvinegar sebacate, Aladdin, Sigma-Aldrich); 0.55 w% Na-TFPB (tetri (3, 5-bis (trifluoromethyl) phenyl) sodium borate, Sigma-Aldrich); 33 wt.% PVC (polyvinyl chloride, Aladdin). After the mixture of the above reagents is formed, 200 mg of the mixture was dissolved in 1320 µl tetrahydrofuran, and 4 µl drops were applied to the electrode surface, and sodium ion selective electrode was prepared after drying. The voltage path of the ion was tested by the voltage regulator input of the CHI660E electrochemical workstation at 0.1–1 V (step 0.1 V).

Animal Culture and Grouping: The experiments were performed on 42 Kunming mice (female, 8 weeks, 30–35 g) without any skin diseases. Mice were kept in the animal center of the Beijing Institute of Nanoenergy and Nanosystems without pathogens at 25 °C. All experimental procedures were reviewed and approved by the University Committee on Animal Resources.

Animal Experiment: The back hair of mice was removed with an electric hair clipper and hair removal cream. A mouse full-layer skin wound model (circular defect with a diameter of 10 mm) was established, and droplets of 0.9% NaCl solution were added to the wounds of Kunming mice to simulate burns or extensive trauma patients with a large amount of exudate. Thirty-six mice were randomly divided into 3 groups: PU group, C/PU group and smig-EESD group. Only dressing was used for wound surface in the PU group. The mice in the C/PU group were coated with PU dressing containing carbon with low sodium storage properties, and the carbon content in the dressing was 1.5% w/w. The mice in the smig-EESD group were coated with PU dressing containing 1.5% w/w HC. PBS was used to simulate exudate, with 3 ml of PBS being slowly dripped into the wound over 3 h and absorbed by the dressing. Wound morphology was

observed and recorded by digital camera at day 0, 3, 6, 9, 11, and 30. Image J was used to measure the wound area. At day 3, 11 and 30, wound tissue was collected for observation and analysis. wound area (%) = [wound area/initial wound area] × 100.

The chronic wound model was established on the back of diabetic mice. Kunming mice were fasted for 14 h and then injected with 1 wt.% STZ solution (100 mg kg^{-1}) for three consecutive days. On the 4th day, the blood glucose of mice was tested using a blood glucose meter (Abbott). Mice with blood glucose values not less than 16.1 mmol L^{-1} were considered diabetic mice. The wound modeling method was consistent with that of acute wounds.

Wound Potential Measurement: The 3D colormap surface type maps were the average EF intensity of 81 areas collected on the wound surface. The EF intensity was obtained by separating the positive and negative electrodes of the oscilloscope (Teledyne LeCroy HD 4096) by 1 mm to obtain the potential difference, which was the average EF intensity of the area. Origin 9.0 was applied to draw and smooth into a 3D colormap surface type map. The wound potential was measured by the oscilloscope (Teledyne LeCroy HD 4096). The positive electrode of the potential electrode was placed on the wound edge and the negative electrode was placed on the wound center. In general, 10 s of stable data at each time point was collected as the typical waveform at that time point. The electrodes were encapsulated in UV-curable glue.

Histology: The tissue was soaked in 4% paraformaldehyde and fixed. Dehydrated with gradient ethanol, embedded in paraffin blocks, section thickness of 4 µm. The tissue sections were analyzed by hematoxylin and eosin (H&E), Masson, immunofluorescence and Sirius red staining. In immunofluorescence staining, the sections were closed with 5% sheep serum PBS at room temperature for 1 h. They incubated with anti-CD68 (Abcam, ab125212, 1:200), CD206/Mannose Receptor/MMR Antibody (15-2) (SANTA CRUZ ANIMAL HEALTH, 1:200) and iNOS Antibody (C-11) (SANTA CRUZ ANIMAL HEALTH, 1: 200) overnight, and washed with PBS 3 times. The secondary antibody was added for 1 h (dilution 1:1000), and finally incubated with DAB-H_2O_2 solution for 5 min. After microscope observation, Image J was used to analyze the positive expression rate.

Transcriptome Sequencing and Data Analysis: The wound tissue was collected for 6 days, and RNA was extracted from the wound tissue by an RNA extraction kit (ACMEC, AR1200). RNA-seq was performed by Illumina HiSeq X10 (Illumina, USA). Novogene (Beijing, China) conducted the quality control, comparison, and quantification of raw RNA-seq data. R (Version 3.0.3) was used for conducting RNA-seq expression data analysis was conducted. A minimum two- fold change and a Padj cutoff of less than 0.05 was applied as filtering criteria.

qPCR Assay: HaCaT cells were co-cultured with 5 mg ml^{-1} HC and CB for 3 h in 6-well cell plate. Blank group did not add any substance except growth medium. The cells were collected and RNA was extracted with an RNA extraction kit (ACMEC, AR1200). DNA was obtained using a reverse transcription kit. Gene expression was quantified through quantitative PCR (qPCR).

ATP Content Detection: The HaCaT cells co-cultured with 5 mg ml^{-1} HC and CB for 24 h in 12-well cell plate, no intervention as Blank group. The ATP content in HaCaT cells was detected using an ATP Assay Kit (MCE, HY-K0314).

Immunofluorescence: The HaCaT cells co-cultured with 5 mg ml^{-1} HC and CB for 24 h in 12-well cell plate, no intervention as Blank group. The cells were blocked with 3% BSA (Solarbio, SW3015) and 10% FBS (10099-141, Gibco) in 0.3% Triton X-100 (T8200) for 2 h at room temperature, incubated with Anti-Ki67 (ab16667, Abcam,1:2000) and anti-Atp1b1 (ab2873, Abcam,1:200) overnight at 4 °C. The sections incubated with fluorescent secondary antibodies for 1 h (1:1000). Finally, DAPI (1:200, c0060, Solarbio) was used to incubate the sections. The photos were taken with the confocal fluorescence microscope (Leica SP8). Image J was used to analyze the positive expressions.

ELISA Test: NIH3T3 ($5*10^{5}$) cells were seeded in a 24-well plate. Electrical stimulation of 200 mV was applied to the cells to simulate the effect of enhanced endogenous EF of wound on cells. 1 day later, the culture medium of NIH3T3 cells was taken and the content of IL-33 was detected using Mouse IL-33 ELISA Kit (Multisciences, EK233). The OD value was detected at 450 nm using a microplate reader.

Flow Cytometry: Purified T cells were obtained from peripheral blood and spleen of Kunming mice. T cells were cultured with the supernatant of NIH3T3 cells for 3 days. Then, flow cytometry was used to evaluate the expression of CD4 and IL-4 of the T cell. CD4 was quantified by incubating with 0.25 µL APC anti-mouse CD4 Antibody (Biolegend, 100 516) for 30 min. 1 × BD Perm/Wash Buffer was used for T cell fixation and membrane permeabilization. IL-4 was quantified by incubating with 0.25 µL Alexa Fluor 488 anti-mouse IL-4 Antibody (Biolegend, 504 111) for 20 min. All these determinations were performed in the cell quantitative analyzer (BWCKMAN COULTER, BG06024) and analyzed using FlowJo software.

Statistical Analysis: Statistical significance of differences was determined by one-way ANOVA. All cell experiments were repeated three times. In the animal experiment, the injury analysis and statistics of each group were from 6 independent injury conditions of 6 mice. The statistical data of H&E staining, Masson staining, immunofluorescence staining and Sirius red staining of wound tissue in each group were derived from the parallel experimental results of 3 mice. Data were analyzed using the mean ± standard error of mean (S.E.M.) in GraphPad Prism v.8. Data rendering using Image J and Origin 2018. $*p < 0.05$, $**p < 0.01$, and $***p < 0.001$ were considered statistically significant.

Supporting Information

Supporting Information is available from the Wiley Online Library or from the author.

Acknowledgements

The authors are grateful to all the laboratory members for their cooperation in this study. The authors thanks for the support received from National Key R&D project from Minister of Science and Technology (2022YFB3804700), National Natural Science Foundation of China (Nos. T2125003, 52372174, and 82272285), Beijing Natural Science Foundation (L212010 and L245015), and The Fundamental Research Funds for the Central Universities.

Conflict of Interest

The authors declare no conflict of interest.

Author Contributions

J.Z., D.L., and Z.L. conceived the idea and designed the experiment. J.Z., D.L., and Z.L. guided the project. R.L. designed and fabricated the smig-ESSD. Y.F., Y.B.J.L., and M.X. performed the material characterization. R.L. carried out the related electrical characterization. R.L. have processed the data and carried out the cell experiments. R.L. and Y.Q. carried out the animal experiments. R.L. analyzed the data from the animal experiments. R.L. wrote the manuscript. J.Z., D.L., and Z.L. reviewed and edited the manuscript. All authors reviewed and commented on the manuscript.

Data Availability Statement

The data that support the findings of this study are available from the corresponding author upon reasonable request.

Keywords

electric stimulation therapy, endogenic electrical stimulation dressing, hard carbon, ion absorption, wound repair

Received: December 6, 2024
Revised: January 14, 2025
Published online:

[1] C. K. Sen, *Adv. Wound Care* **2021**, *10*, 281.
[2] a) G. S. Schultz, J. M. Davidson, R. S. Kirsner, P. Bornstein, I. M. Herman, *Wound Repair Regener.* **2011**, *19*, 134; b) S. Barrientos, O. Stojadinovic, M. S. Golinko, H. Brem, M. Tomic-Canic, *Wound Repair Regener.* **2008**, *16*, 585.
[3] a) V. Falanga, *Lancet* **2005**, *366*, 1736; b) S. A. Eming, T. Krieg, J. M. Davidson, *J. Invest. Dermatol.* **2007**, *127*, 514.
[4] M. Zhao, *Semin. Cell Dev. Biol.* **2009**, *20*, 674.
[5] a) R. Z. Luo, J. Y. Dai, J. P. Zhang, Z. Li, *Adv. Healthcare Mater.* **2021**, *10*, 2100557; b) Y. Liang, H. Tian, J. Liu, Y. Lv, Y. Wang, J. Zhang, Y. Huang, *Bioelectrochemistry* **2020**, *135*, 107578.
[6] C. Martin-Granados, C. D. McCaig, *Adv. Wound Care* **2014**, *3*, 127.
[7] M. Levin, G. Pezzulo, J. M. Finkelstein, *Annu. Rev. Biomed. Eng.* **2017**, *19*, 353.
[8] a) L. C. Kloth, *Adv. Wound Care* **2014**, *3*, 81; b) Q. Du, S. Su, H. Dai, Z. Li, *Chin. Sci. Bull.* **2024**, *69*, 2008.
[9] a) Y. Jiang, A. A. Trotsyuk, S. Niu, D. Henn, K. Chen, C.-C. Shih, M. R. Larson, A. M. Mermin-Bunnell, S. Mittal, J.-C. Lai, A. Saberi, E. Beard, S. Jing, D. Zhong, S. R. Steele, K. Sun, T. Jain, E. Zhao, C. R. Neimeth, W. G. Viana, J. Tang, D. Sivaraj, J. Padmanabhan, M. Rodrigues, D. P. Perrault, A. Chattopadhyay, Z. N. Maan, M. C. Leeolou, C. A. Bonham, S. H. Kwon, et al., *Nat. Biotechnol.* **2023**, *41*, 652; b) J. W. Song, H. Ryu, W. Bai, Z. Xie, A. Vazquez-Guardado, K. Nandoliya, R. Avila, G. Lee, Z. Song, J. Kim, M.-K. Lee, Y. Liu, M. Kim, H. Wang, Y. Wu, H.-J. Yoon, S. S. Kwak, J. Shin, K. Kwon, W. Lu, X. Chen, Y. Huang, G. A. Ameer, J. A. Rogers, *Sci. Adv.* **2023**, *9*, ade4687.
[10] a) M. Li, X. Wang, P. Rajagopalan, L. Zhang, S. Zhan, S. Huang, W. Li, X. Zeng, Q. Ye, Y. Liu, K. Zhong, J. M. Kim, J. Luo, S. Dong, R. Gu, X. Wang, W.-Q. Tan, *ACS Appl. Bio Mater.* **2020**, *3*, 8901; b) W. Besio, V. Sharma, J. Spaulding, *Ann. Biomed. Eng.* **2010**, *38*, 1111; c) P. Li, J. Xu, Q. Shi, J. Wang, W. Zhang, L. Zheng, M. Wang, Y. Fan, *Adv. Wound Care* **2023**, *12*, 498.
[11] R. Z. Luo, Y. Liang, J. R. Yang, H. Q. Feng, Y. Chen, X. P. Jiang, Z. Zhang, J. Liu, Y. Bai, J. T. Xue, S. Y. Chao, Y. Xi, X. Q. Liu, E. G. Wang, D. Luo, Z. Li, J. P. Zhang, *Adv. Mater.* **2023**, *35*, 2208395.
[12] N. Sun, Z. Guan, Y. Liu, Y. Cao, Q. Zhu, H. Liu, Z. Wang, P. Zhang, B. Xu, *Adv. Energy Mater.* **2019**, *9*, 1901351.
[13] Z. Tian, Y. Zhang, J. Zhu, Q. Li, T. Liu, M. Antonietti, *Adv. Energy Mater.* **2021**, *11*, 2102489.
[14] Y. Li, Y.-S. Hu, M.-M. Titirici, L. Chen, X. Huang, *Adv. Energy Mater.* **2016**, *6*, 1600659.
[15] a) D. A. Stevens, J. R. Dahn, *J. Electrochem. Soc.* **2001**, *148*, A803; b) P. Bai, Y. He, X. Zou, X. Zhao, P. Xiong, Y. Xu, *Adv. Energy Mater.* **2018**, *8*, 1703217.
[16] a) A. Gefen, P. Alves, D. Beeckman, J. L. Lazaro-Martinez, H. Lev-Tov, B. Najafi, T. Swanson, K. Woo, *Int. Wound J.* **2023**, *20*, 1960; b) C. Wang, E. S. Sani, C.-D. Shih, C. T. Lim, J. Wang, D. G. Armstrong, W. Gao, *Nat. Rev. Mater.* **2024**, *9*, 550.
[17] C. T. McKee, J. A. Last, P. Russell, C. J. Murphy, *Tissue Eng. Part B Rev.* **2011**, *17*, 155.
[18] R. Luo, B. Shi, D. Luo, Z. Li, *Sci. Bull.* **2023**, *68*, 1740.
[19] K. Y. Nishimura, R. R. Isseroff, R. Nuccitelli, *J. Cell Sci.* **1996**, *109*, 199.
[20] A. J. Singer, R. A. F. Clark, *N. Engl. J. Med.* **1999**, *341*, 738.
[21] E. Tokhtaeva, G. Sachs, O. Vagin, *J. Biol. Chem.* **2010**, *285*, 39289.
[22] A. L. Sugden, B. L. Bean, J. A. Straw, *Hypertension* **1987**, *9*, 571.
[23] S. Q. Liu, Y. H. Hur, X. Cai, Q. Cong, Y. H. Yang, C. W. Xu, A. M. Bilate, K. A. U. Gonzales, S. M. Parigi, C. J. Cowley, B. Hurwitz, J. D. Luo, T. Tseng, S. Gur-Cohen, M. Sribour, T. Omelchenko, J. Levorse, H. A. Pasolli, C. B. Thompson, D. Mucida, E. Fuchs, *Cell* **2023**, *186*, 2127.
[24] a) M. Manetti, L. Ibba-Manneschi, V. Liakouli, S. Guiducci, A. F. Milia, G. Benelli, A. Marrelli, M. L. Conforti, E. Romano, R. Giacomelli, M. Matucci-Cerinic, P. Cipriani, *Ann. Rheum. Dis.* **2010**, *69*, 598; b) E. Adami, S. Viswanathan, A. A. Widjaja, B. Ng, S. Chothani, N. Zhihao, J. Tan, P. M. Lio, B. L. George, U. Altunoglu, K. Ghosh, B. S. Paleja, S. Schafer, B. Reversade, S. Albani, A. L. H. Ling, S. O'Reilly, S. A. Cook, *Rheumatology* **2021**, *60*, 5820.
[25] J. N. Buzzelli, H. V. Chalinor, D. I. Pavlic, P. Sutton, T. R. Menheniott, A. S. Giraud, L. M. Judd, *Cell. Mol. Gastroenterol. Hepatol.* **2015**, *1*, 203.
[26] C. D. Mills, *Front. Immunol.* **2015**, *6*, 212.
[27] H. Kim, S. Y. Wang, G. Kwak, Y. Yang, I. C. Kwon, S. H. Kim, *Adv. Sci.* **2019**, *6*, 1900513.
[28] M. W. J. Ferguson, S. O'Kane, *Philos. Trans. R Soc. Lond B Biol. Sci.* **2004**, *359*, 839.
[29] a) X. W. Xu, S. C. Gu, X. Huang, J. Y. Ren, Y. H. Gu, C. J. Wei, X. Lian, H. Z. Li, Y. S. Gao, R. Jin, B. Gu, T. Zan, Z. C. Wang, *Burns & Trauma* **2020**, *8*, tkaa006; b) L. Chen, J. Wang, S. Li, Z. Yu, B. Liu, B. Song, Y. Su, *Int. Wound J.* **2019**, *16*, 360.
[30] M. Xue, C. J. Jackson, *Adv. Wound Care* **2015**, *4*, 119.
[31] T. Hurme, H. Kalimo, M. Sandberg, M. Lehto, E. Vuorio, *Lab. Invest.* **1991**, *64*, 76.
[32] J. C. Dallon, J. A. Sherratt, P. K. Maini, *Wound Repair Regener.* **2001**, *9*, 278.